DALTON
FULL PAPER

Chalcogenide-bridged ditungsten (M–M) complexes: an experimental and theoretical study of the electronic structure and bonding in $W_2(\mu\text{-}E)(\mu\text{-}OCH_2{}^tBu)_2(OCH_2{}^tBu)_6$, where E = O, S, Se or Te †

John C. Bollinger,[a] Malcolm H. Chisholm,[b] Damon R. Click,[a] Kirsten Folting,[a] Christopher M. Hadad,[b] Darin B. Tiedtke[a] and Paul J. Wilson[b]

[a] *Department of Chemistry and Molecular Structure Center, Indiana University, Bloomington, IN 47405, USA*
[b] *Department of Chemistry, The Ohio State University, Newman & Wolfrom Laboratories, 100 W. 18th Avenue, Columbus, OH 43210, USA*

Received 12th February 2001, Accepted 10th May 2001
First published as an Advance Article on the web 25th June 2001

The series of compounds $W_2(\mu\text{-}E)(\mu\text{-}OCH_2{}^tBu)_2(OCH_2{}^tBu)_6$, where E = O, S, Se, or Te, has been isolated from the reactions between $[W_2(OCH_2{}^tBu)_8]_n$ and pyridine *N*-oxide, elemental sulfur, elemental selenium and tri-*n*-butylphosphine telluride. The reactions were carried out in hexane or toluene solutions, and the new compounds were isolated as crystalline products by recrystallization from hexanes at low temperatures (E = O, S, Se) or from hot toluene (E = Te). Each compound displays temperature-dependent ^{1}H NMR spectra indicative of bridge $\rightleftharpoons$ terminal alkoxide group exchange which is frozen out at *ca.* −65 °C. The low-temperature spectra are consistent with the observed molecular structures in the solid state as determined by single-crystal X-ray studies. There is a central $O_3M(\mu\text{-}O)_2(\mu\text{-}E)MO_3$ skeleton having virtual C_{2v} symmetry. The W–W internuclear distances range from 2.55 to 2.66 Å and gradually increase along the series O → S → Se → Te. The compounds are colored (E = O: violet; E = S: blue; E = Se: blue-green; and E = Te: dark yellow/amber) as a result of absorptions in the visible region of the spectrum. The electronic structures of these compounds have been investigated using density functional theory (DFT) by examining the model compounds $W_2(\mu\text{-}E)(\mu\text{-}OCH_3)_2(OCH_3)_6$ (E = O, S, Se, or Te). These B3LYP(SDD,6-31G*) calculations reveal that the HOMO is a M–M σ-type molecular orbital, and with increasing mass of E, the orbital energies of the Ep_π lone-pair orbitals approach this level. A tentative assignment of the electronic absorption spectra is made on the basis of time-dependent DFT (TDDFT) calculations.

Introduction

The chemistry of metal–metal (M–M) double bonds is much less developed than that for M–M quadruple and triple bonds.[1] In dinuclear chemistry, the only two systems to have been studied extensively are $Cp^*_2Re_2(CO)_4$[2] and $Os_2(CO)_8$.[3] The d^2–d^2 complex $[W_2(OCH_2{}^tBu)_8]_n$, which contains a W–W double bond, was first synthesized in 1995.[4] $[W_2(OCH_2{}^tBu)_8]_n$ is insoluble in non-coordinating hydrocarbon solvents such as hexane and toluene and has a polymeric solid-state structure perhaps akin to that recently reported for WCl_4.[5a,b] Despite its polymeric nature, $[W_2(OCH_2{}^tBu)_8]_n$ behaves as a source of $W_2(OCH_2{}^tBu)_8$ in its reactions with small unsaturated molecules leading to an extensive organometallic chemistry as illustrated in Scheme 1 below.[6a,b] In this report we wish to describe the reactivity of $[W_2(OCH_2{}^tBu)_8]_n$ towards the chalcogenide (Group 16) elements and present an experimental and theoretical study of the electronic structure and bonding in the complexes $W_2(\mu\text{-}E)(\mu\text{-}OCH_2{}^tBu)_2(OCH_2{}^tBu)_6$ (E = O, S, Se or Te), which provide a rare example of a homologous series of the Group 16 elements' addition products to M–M multiple bonds.

† Electronic supplementary information (ESI) available: selected bond distances and angles for the title compounds and ground state DFT vertical excitation energies for $W_2(\mu\text{-}E)(\mu\text{-}OCH_3)_2(OCH_3)_6$ (E = O, S, Se or Te). See http://www.rsc.org/suppdata/dt/b1/b101346g/

Results and discussion

Preparations

$[W_2(OCH_2{}^tBu)_8]_n$ reacts with O_2 in hydrocarbon solutions to give $WO(CH_2{}^tBu)_4$ in what may be viewed as a metathetic reaction involving double bonds: M=M + O=O → 2 M=O.[6b] However, the known oxygen-atom transfer reagent pyridine *N*-oxide, pyO, and $[W_2(OCH_2{}^tBu)_8]_n$ react smoothly to give $W_2(\mu\text{-}O)(\mu\text{-}OCH_2{}^tBu)_2(OCH_2{}^tBu)_6$, as a purple crystalline solid upon crystallization from cold hexanes (see eqn. (1)).

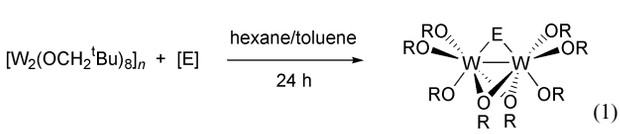

(1)

[E] = pyridine-*N*-oxide, 1/8 S_8, Se or $^nBu_3PTe$

E = O, S, Se, or Te

$[W_2(OCH_2{}^tBu)_8]_n$ and elemental sulfur react similarly to give $W_2(\mu\text{-}S)(OCH_2{}^tBu)_2(OCH_2{}^tBu)_6$ as a blue solid upon crystallization from cold hexanes. A preliminary report has appeared containing the oxo- and sulfido-bridged compounds.[6c]

The selenium analogue can be prepared in hexane solutions and is blue-green in the solid state while the preparation of $W_2(\mu\text{-}Te)(OCH_2{}^tBu)_2(OCH_2{}^tBu)_6$ involving elemental tellurium

 DOI: 10.1039/b101346g

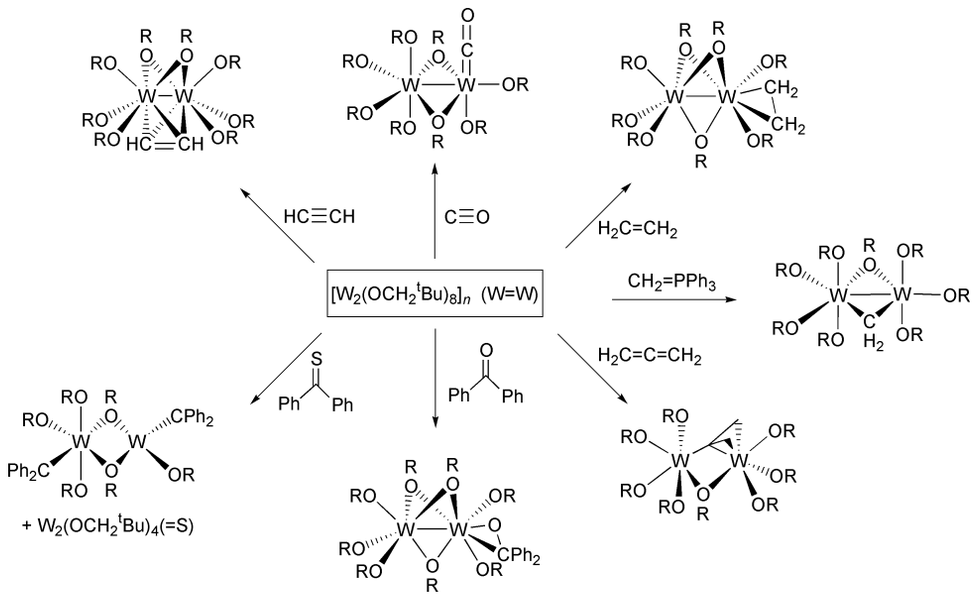

Scheme 1 Summary of reactions previously reported for $[W_2(OCH_2{}^tBu)_8]_n$.[6a,b]

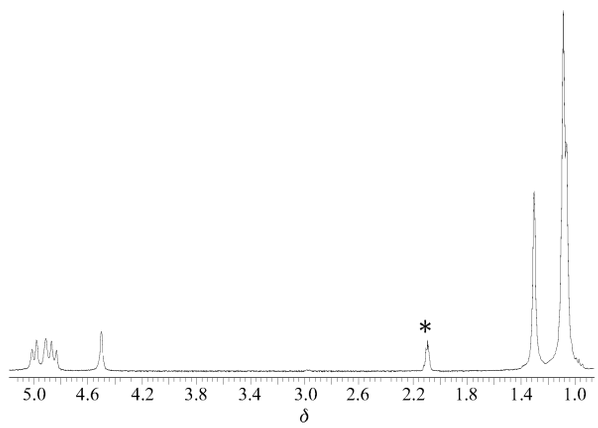

Fig. 1 ^{1}H NMR spectrum of $W_2(\mu\text{-Se})(\mu\text{-}OCH_2{}^tBu)_2(OCH_2{}^tBu)_6$ in toluene-d_8 at −85 °C, 300 MHz. The protio impurity of the toluene-d_8 methyl signal is represented by *.

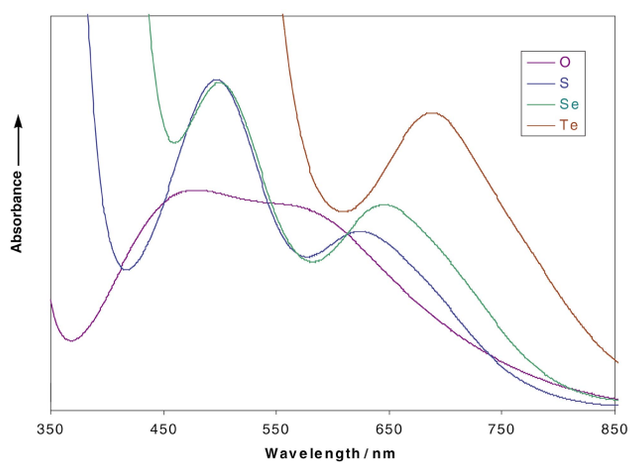

Fig. 2 Comparison of the electronic absorption spectra of the $W_2(\mu\text{-E})(\mu\text{-}OCH_2{}^tBu)_2(OCH_2{}^tBu)_6$ compounds (E = O, S, Se, Te) in the visible region, recorded as THF solutions at room temperature.

in toluene required the use of P^nBu_3 as an atom-transfer catalyst. The tellurido-bridged compound is dark-yellow or amber in solution but is essentially black in the crystalline state because of absorptions across the visible region of the spectrum, *vide infra*.

Physical and spectroscopic properties

The new compounds are air- and moisture-sensitive, diamagnetic and display similar variable-temperature NMR behavior. At room temperature, the spectra of all four compounds show a time-averaged spectrum corresponding to one type of neopentoxy ligand. This simple spectrum, consisting of a singlet for the CH_2 protons at *ca.* δ 4.7 and a singlet for the ^{t}Bu protons at *ca.* δ 1.1, broadens upon lowering the temperature in toluene-d_8 until at −85 °C (300 MHz), a spectrum akin to that shown in Fig. 1 (for E = Se) is observed. There are three ^{t}Bu singlets in the ratio 4 : 2 : 2 and two methylene singlets of equal intensity (4 : 4) and an AB quartet of relative intensity 8. The former can be assigned to two sets of OR ligands: (i) those that are both terminal and *trans* to the W–E bonds or (ii) those that are bridging μ-OR ligands. Both of these sets of OR groups lie on a mirror plane of symmetry. The remaining four alkoxides, which are terminal and symmetry equivalent in the C_{2v} point group, contain diastereotopic methylene protons that give rise to an AB quartet.

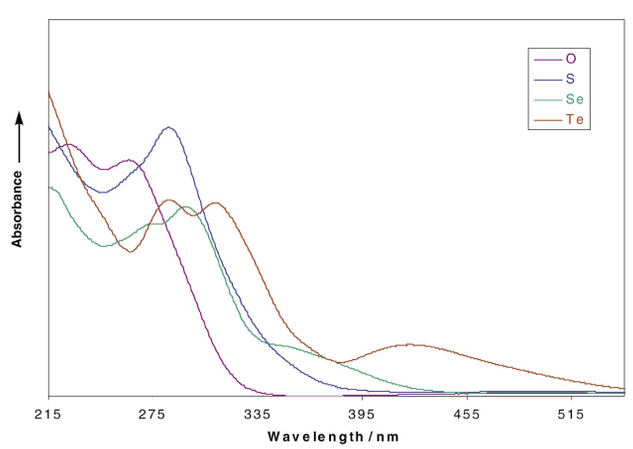

Fig. 3 Comparison of the electronic absorption spectra of the $W_2(\mu\text{-E})(\mu\text{-}OCH_2{}^tBu)_2(OCH_2{}^tBu)_6$ compounds (E = O, S, Se, Te) in the region 215 to 515 nm, recorded as THF solutions at room temperature.

The electronic absorption spectra of the series of compounds are compared in Figs. 2 and 3. In the visible region of the spectra, Fig. 2, each compound shows two partially resolved absorptions which shift to lower energy from O → S → Se → Te. The lowest energy transition retains approximately

Table 1 Summary of crystallographic data for the $W_2(\mu\text{-E})(\mu\text{-OCH}_2{}^t\text{Bu})_2(\text{OCH}_2{}^t\text{Bu})_6$ compounds where E = O, S, Se, or Te

Formula	$C_{40}H_{88}O_9W_2$	$C_{40}H_{88}O_8SW_2$	$C_{40}H_{88}O_8SeW_2$	$C_{40}H_{88}O_8TeW_2$
FW/g mol^{-1}	1081.81	1096.88	1143.77	1192.39
Crystal system	Triclinic	Triclinic	Triclinic	Triclinic
Space group	$P\bar{1}$	$P\bar{1}$	$P\bar{1}$	$P\bar{1}$
a/Å	12.221(1)	14.755(6)	12.258(2)	12.458(5)
b/Å	19.820(2)	14.888(6)	14.780(3)	14.694(6)
c/Å	11.593(1)	12.172(5)	14.777(3)	14.772(6)
α/°	91.56(1)	92.20(2)	93.239(5)	93.73(1)
β/°	111.49(1)	113.17(2)	113.413(5)	113.95(1)
γ/°	72.05(1)	93.03(2)	91.936(5)	90.99(1)
V/Å^3	2474.00	2449.60	2448.15	2463.07
Z	2	2	2	2
T/K	108	108	113	114
λ/Å	0.71069	0.71069	0.71073	0.71073
μ/cm^{-1}	46.949	47.825	54.863	59.947
Unique data	6890	6376	13788	10392
Observed data	10464	8889	41540	39903
$R(F)$	0.0228	0.0294	0.0472	0.0444
$Rw(F)$	0.0266	0.0312	$Rw(F^2)$ 0.1214	$Rw(F^2)$ 0.1109

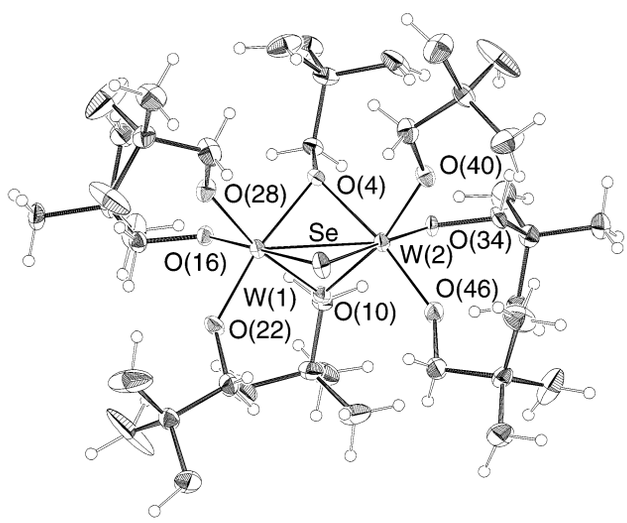

Fig. 4 An ORTEP[26] drawing of the molecular structure of the $W_2(\mu\text{-Se})(\mu\text{-OCH}_2{}^t\text{Bu})_2(\text{OCH}_2{}^t\text{Bu})_6$ molecule. Thermal ellipsoids are drawn at the 50% probability level.

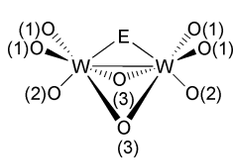

Fig. 5 The atom numbering scheme used in Table 2 for the $W_2(\mu\text{-E})(\mu\text{-O})_2(O)_6$ core for the $W_2(\mu\text{-E})(\mu\text{-OCH}_2{}^t\text{Bu})_2(\text{OCH}_2{}^t\text{Bu})_6$ molecules (E = O, S, Se, Te).

the same molar absorptivity throughout the series $\varepsilon \approx 170$–340 dm^3 mol^{-1} cm^{-1}, whereas the higher energy absorption in the visible region gains in intensity from O → Te ($\varepsilon \approx 220$–5500 dm^3 mol^{-1} cm^{-1}). Above 300 nm, there are intense absorptions which are clearly ligand-to-metal charge-transfer, LMCT, in nature but which vary significantly with the nature of E. These features will be discussed later.

Solid-state and molecular structures

All four compounds have been examined by single-crystal X-ray diffraction, and a summary of the crystal data is given in Table 1. All of the compounds share a common structural motif involving face-shared octahedra $O_3M(\mu\text{-O})_2(\mu\text{-E})MO_3$. Though there is no crystallographically imposed symmetry, each of the molecules has virtual C_{2v} symmetry. A view of the selenido-bridged structure is shown in Fig. 4. Given the common core and the atom numbering scheme used in Fig. 5, we can compare the experimental and the B3LYP(SDD, 6-31G*) calculated average bond distances and angles for the W_2O_8E cores as shown in Table 2 (complete data are available in the supplementary information). The following significant points emerge from an inspection of Table 2: (1) The W–E distances increase with increasing atomic number of E as do the W–W distances which range from 2.55 to 2.66 Å. (2) The W–E–W angle decreases down the series O > S > Se > Te and values span the range of 81.3° to 59.2°. (3) The W–O(3) distances involving the bridging OR ligands are longer than those to the terminal OR groups, W–O(1) and W–O(2) as expected. (4) For the terminal ligands, the W–O(2) distances are longer than the W–O(1) distances implying a greater *trans*-influence order of μ-E > μ-OR. Within the homologous series W–O(2) is longest for the tellurido-bridged complex and shortest for the oxo-bridged complex implying that the *trans*-influence order of the μ-E ligands follows the series Te > Se > S > O.

Electronic structure considerations

Based on the diamagnetism of the complexes and the W–W distances, which range from 2.55 to 2.66 Å, it seems reasonable to suppose that the complexes possess a W–W single bond. Also, from the electronic absorption spectra, we considered that the lowest energy absorption may arise from an electronic transition of a M–M σ-orbital to a higher energy M–M unoccupied orbital. In addition, we postulated that there would be a transition from an occupied orbital consisting mainly of Ep_π lone-pair character to a higher energy M–M unoccupied orbital. In order to investigate the electronic structure further, we carried out calculations employing density functional theory (DFT) with the Gaussian 98 program, at the B3LYP(SDD, 6-31G*) level, on the model compounds $W_2(\mu\text{-E})(\text{OCH}_3)_2(\text{OCH}_3)_6$ (E = O, S, Se, or Te). For the oxo-, sulfido- and selenido-bridged compounds, the geometry was optimized in the C_{2v} symmetry group. The tellurido-bridged compound was optimized under C_s symmetry due to convergence problems, and the geometry was considered optimized when the total energy (in Hartrees), stopped changing in the fifth decimal place. In addition we have made acceptable comparisons throughout this manuscript with regard to the frontier molecular orbitals obtained from the calculations having rigorous C_{2v} symmetry and the tellurido-bridged complex having C_s symmetry.

A frontier orbital energy level diagram for the series, O → Te, based upon DFT ground state orbital energies is shown in Fig. 6, where it can be seen that with increasing atomic number of E, the energy gaps between the HOMO and the LUMO and LUMO + 1 decrease. Also, the HOMO is determined to be of a_1 symmetry (a′ for Te) in each case and is predominantly M–M σ-bonding. The σ-bond is comprised of the tungsten d_{z^2} orbitals. The HOMO − 1 orbital is an E-based

Table 2 Comparison of the observed and calculated structural parameters of the $W_2(\mu\text{-}E)(\mu\text{-}O)_2(O)_6$ core for the $W_2(\mu\text{-}E)(\mu\text{-}OCH_2{}^tBu)_2(OCH_2{}^tBu)_6$ and $W_2(\mu\text{-}E)(\mu\text{-}OCH_3)_2(OCH_3)_6$ molecules, respectively, where E = O, S, Se or Te

		μ-O	μ-S	μ-Se	μ-Te
W–W/Å	Exp.	2.5509(4)	2.628(1)	2.6414(7)	2.662(1)
	Calc.	2.60	2.69	2.70	2.72
W–E/Å	Exp.	1.958(3)	2.355(2)	2.485(1)	2.694(2)
	Calc.	2.00	2.42	2.59	2.78
W–O(1)/Å avg.	Exp.	1.88(3)	1.879(2)	1.87(1)	1.91(2)
	Calc.	1.91	1.91	1.91	1.90
W–O(2)/Å avg.	Exp.	1.929(3)	1.937(3)	1.937(8)	1.94(1)
	Calc.	1.95	1.96	1.96	1.96
W–O(3)/Å avg.	Exp.	2.104(2)	2.090(2)	2.081(9)	2.08(2)
	Calc.	2.11	2.11	2.10	2.10
W–E–W/°	Exp.	81.27(1)	67.82(5)	64.21(2)	59.20(3)
	Calc.	81.08	67.28	62.89	58.92
E–W–O(2)/° avg.	Exp.	164.9(2)	178.7(1)	178.2(2)	176.9(3)
	Calc.	177.1	177.8	178.0	178.2
O(1)–W–O(1)/° avg.	Exp.	102.3(2)	102.7(2)	102.6(3)	103.3(4)
	Calc.	99.7	101.0	101.3	100.7
O(3)–W–O(3)/° avg.	Exp.	75.9(2)	74.8(2)	74.7(3)	73.7(4)
	Calc.	78.3	77.8	78.2	78.0
E–W–O(1)/° avg.	Exp.	89.6(2)	91.5(2)	90.9(3)	90.4(5)
	Calc.	91.8	92.8	92.7	92.7
W–O(3)–W/° avg.	Exp.	74.6(1)	77.9(2)	78.8(2)	79.6(4)
	Calc.	75.8	79.2	79.9	80.5

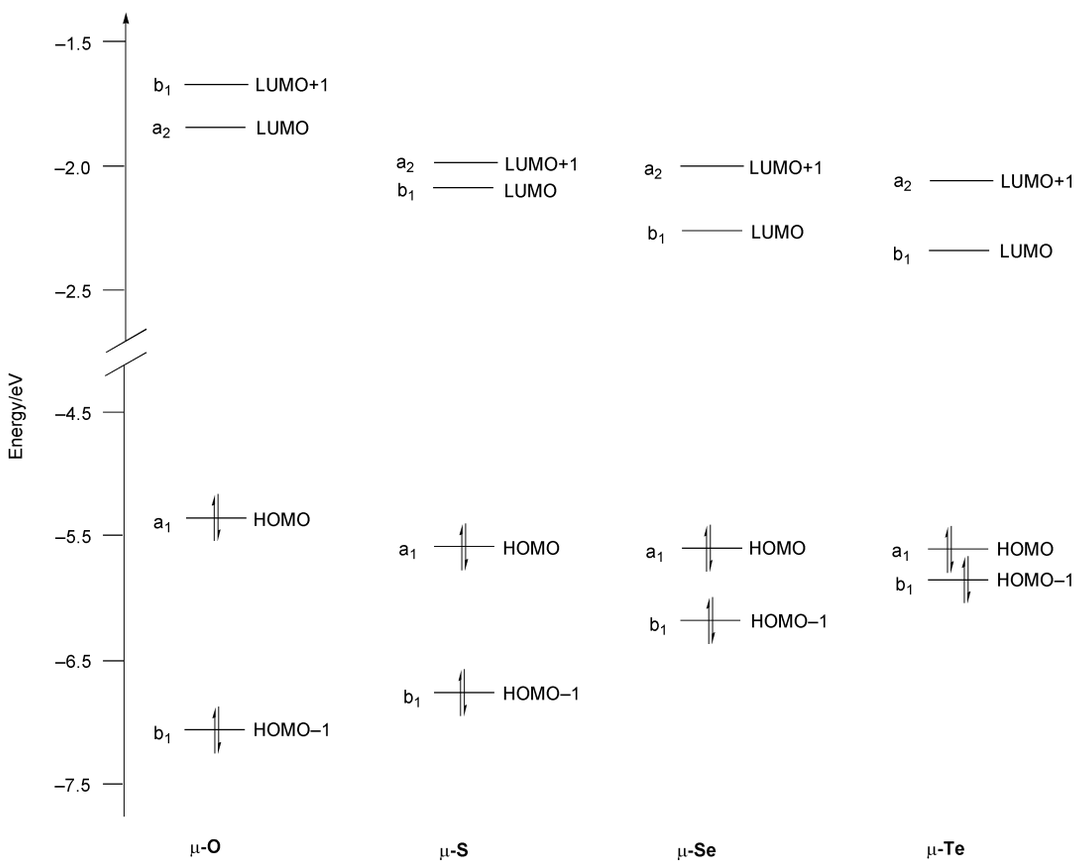

Fig. 6 A comparison of the calculated frontier orbital energies of the $W_2(\mu\text{-}E)(\mu\text{-}OCH_3)_2(OCH_3)_6$ molecules (E = O, S, Se, Te).

p_π orbital, b_1 in C_{2v} (a″ in C_s for Te), and this orbital is raised in energy down the series from O → Te. The lowest energy frontier orbitals that are unoccupied are of a_2 and b_1 symmetry (both are a″ for Te). The a_2 (a″ for Te) orbital is an out-of-phase M–M π-type MO. The b_1 orbital is higher in energy than the a_2 orbital for the oxo-bridged complex (Fig. 6), and this order changes upon moving to the sulfido-bridged complex and further to Se and Te. The subsequent drop in energy of the b_1 orbital descending the series from O → Te (see Fig. 6) can be attributed to the changing nature of the unoccupied b_1 orbital. The unoccupied b_1 orbital consists of a M–M d_π in-phase combination that is out-of-phase with respect to the Ep_π orbital, which is perpendicular to the metal–metal axis. Descending the series from O → Te, the W–E distances get longer (Table 2), and the b_1 orbital is lowered in energy. A complete list of the ground state DFT calculated orbital energies with frontier orbital transition energies is given in the supplementary information.

The DFT calculations agree with what might have been qualitatively predicted, namely that with increasing W–W distance, the lowest energy virtual orbitals fall in energy such that the HOMO–LUMO gap decreases down the series. Also with

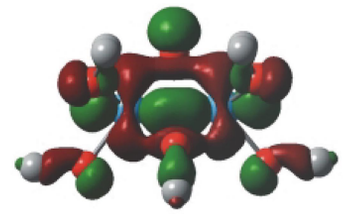

HOMO a_1

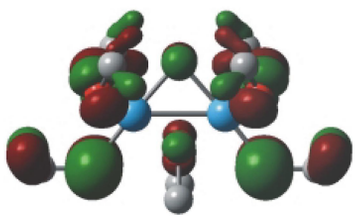

HOMO–1 b_1

Fig. 7 Molecular orbital plots for the HOMO and HOMO − 1 of $W_2(\mu\text{-}O)(\mu\text{-}OCH_3)_2(OCH_3)_6$.

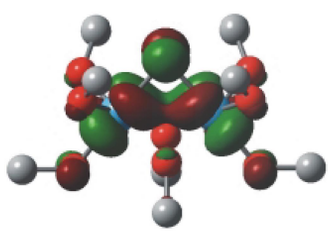

LUMO+1 b_1

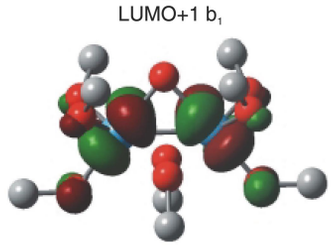

LUMO a_2

Fig. 8 Molecular orbital plots for the LUMO and LUMO + 1 of $W_2(\mu\text{-}O)(\mu\text{-}OCH_3)_2(OCH_3)_6$.

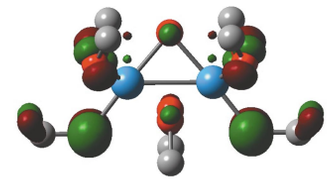

E = O

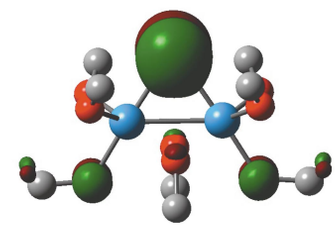

E = S

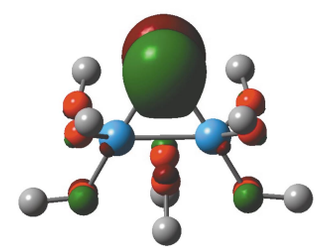

E = Se

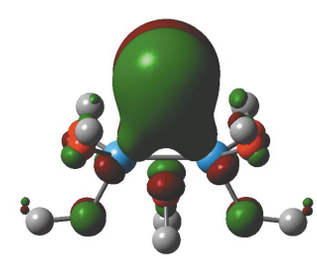

E = Te

Fig. 9 Comparison of the Ep_π (HOMO − 1) molecular orbital perpendicular to the $W_2(\mu\text{-}E)$ plane.

decreasing electronegativity of the chalcogenide element down the series, we would expect that the Ep_π orbitals would be raised in relative energy.

The occupied frontier molecular orbitals of the oxo-bridged compound are shown in Fig. 7 and the LUMO (a_2) and LUMO + 1 (b_1) orbitals are shown in Fig. 8. A comparison of the Ep_π-based MOs, the occupied b_1 orbital (a″ for Te), for the series O → Te is shown in Fig. 9 and reveals how the HOMO − 1 orbital becomes increasingly localized on the E atom.

In the C_{2v} point group, the a_1 to a_2 electronic transition is forbidden. Thus, the HOMO to LUMO transition is forbidden for the oxo-bridged complex, but the HOMO (a_1) to LUMO + 1 (b_1) transition is symmetry allowed. The electronic transitions from the HOMO − 1 (b_1), the Ep_π orbital (Fig. 9), to the LUMO (a_2) and LUMO + 1 (b_1) orbitals are also both allowed. For the sulfido-, selenido-, and tellurido-bridged complexes, the HOMO (a_1) (a′ for Te) to LUMO (b_1) (a″ for Te) electronic transition is symmetry allowed, but the HOMO (a_1) to LUMO + 1 (a_2) electronic transition is forbidden for the sulfido- and selenido-bridged complexes. The HOMO (a′) to LUMO + 1 (a″) transition for the tellurido-bridged complex is allowed by symmetry. The electronic transitions from the HOMO − 1 (b_1) (a″ for Te), the Ep_π orbital, to the LUMO (b_1) (a″ for Te) and LUMO + 1 (a_2) orbitals are symmetry allowed for the sulfido-, selenido- and tellurido-bridged complexes.

In an attempt to calculate the electronic absorption spectra of this series of molecules and to show how these are correlated with the changing nature of E, we utilized time-dependent DFT (TDDFT).[7a,b] The pertinent, calculated vertical excitation energies (in eV and nm) using this method are given in Table 3 along with the experimentally observed absorption bands. A more complete listing of the calculated electronic transitions for these compounds is provided in the supplementary information.

The HOMO (a_1) to LUMO (a_2) transition for the oxo-bridged complex is forbidden under C_{2v} symmetry, and thus the predicted TDDFT oscillator strength for this transition is zero. However, the HOMO (a_1) to LUMO + 1 (b_1) and HOMO (a_1) to LUMO + 2 (b_1) transitions are symmetry allowed. The LUMO + 1 orbital, as mentioned earlier, consists of a M–M d_π in-phase combination (the metal's d_{xy} orbitals) that is out-of-phase with respect to the Ep_π orbital, which is perpendicular to the metal–metal axis (see Fig. 8). The LUMO + 2 orbital is an out-of-phase M–M δ-type orbital (the metal's $d_{x^2-y^2}$ orbitals) that is in-phase with an Ep_π orbital, which is parallel to the M–M axis. The experimentally obtained λ_{max} values for the two lowest energy bands are at 568 nm (2.18 eV) and 478 nm (2.59 eV). The calculated λ_{max} values are 538 nm (2.31 eV) and 534 nm (2.32).

Table 3 Comparison of the transition energies calculated using TDDFT for $W_2(\mu\text{-}E)(\mu\text{-}OCH_3)_2(OCH_3)_6$ (E = O, S, Se, Te)

Transition	Weight of transition	Oscillator strength	Calculated λ_{max} values and excitation energies		Observed λ_{max} values and excitation energies	
			λ/nm	λ/eV	λ/nm	λ/eV
$W_2(\mu\text{-}O)(\mu\text{-}OCH_3)_2(OCH_3)_6$						
$30a_1$(HOMO) → $23b_2$(LUMO + 2)	0.68277	0.0006	538	2.31	568	2.18
$30a_1$(HOMO) → $21b_1$(LUMO + 1)	0.68046	0.0001	534	2.32	478	2.59
Charge transfer bands	—	0.0–0.1278	302–261	4.10–4.75	261, 226	4.75, 5.49
$W_2(\mu\text{-}S)(\mu\text{-}OCH_3)_2(OCH_3)_6$						
$32a_1$(HOMO) → $22b_1$(LUMO)	0.67993	0.0010	553	2.24	625	1.98
$32a_1$ → $24b_2$(LUMO + 2)	0.67003	0.0008	502	2.47	498	2.49
$32a_1$ → $25b_2$(LUMO + 4)	0.15382					
Charge transfer bands	—	0.0–0.1244	353–290	3.51–4.27	284, 265	4.63, 4.68
$W_2(\mu\text{-}Se)(\mu\text{-}OCH_3)_2(OCH_3)_6$						
$29a_1$(HOMO) → $20b_1$(LUMO)	0.67979	0.0015	566	2.19	645	1.94
$29a_1$(HOMO) → $23b_2$(LUMO + 2)	0.66194	0.0008	509	2.43	499	2.48
$29a_1$ → $24b_2$(LUMO + 4)	0.17730					
$22b_2$(HOMO − 2) → $23b_2$	0.41270	0.0212	359	3.46	345	3.59
$22b_2$ → $24b_2$	0.15858					
$19b_1$(HOMO−1) → $20b_1$	0.51703					
Charge transfer bands	—	0.00–0.1048	330–293	3.76–4.23	294, 276	4.22–4.49
$W_2(\mu\text{-}Te)(\mu\text{-}OCH_3)_2(OCH_3)_6$						
51a′(HOMO) → 35a″(LUMO)	0.67655	0.0020	582	2.12	687	1.80
51a′ → 52a′(LUMO + 2)	0.64361	0.0007	506	2.48	not observed	—
51a′ → 54a′(LUMO + 4)	0.20760					
50a′(HOMO − 2) → 52a′	0.36350	0.0235	414	2.99	423	2.93
50a′ → 54a′	0.15831					
34a″(HOMO − 1) → 35a″	0.54973					
Charge transfer bands	—	0.0–0.0948	362–300	3.42–4.13	310, 284	4.00, 4.36

The TDDFT calculations predict the two lowest energy bands for the sulfido-bridged complex to arise from the HOMO (a_1) to LUMO (b_1) and HOMO to LUMO + 2 (b_2) and HOMO to LUMO + 4 (b_2) transitions. The LUMO + 2 (b_2) orbital is an out-of-phase M–M δ-type orbital that is in-phase with respect to the bridging chalcogenide ligand. The LUMO + 4 (b_2) orbital is an out-of-phase M–M σ-type orbital. The HOMO (a_1) to LUMO (b_1) transition is calculated to be at 553 nm (2.24 eV) and, indeed, a band is observed at 625 nm (1.98 eV). The HOMO to LUMO + 2 (b_2) and HOMO to LUMO + 4 (b_2) transitions are both predicted to be at 502 nm (2.47 eV), and there is a band observed at 498 nm (2.49 eV) in the visible spectrum.

In the case of the selenido-bridged complex, the two lowest energy bands in the visible spectrum are predicted to arise from the HOMO (a_1) to LUMO (b_1) and HOMO to LUMO + 2 (b_2) and HOMO to LUMO + 4 (b_2) transitions. The LUMO + 2 (b_2) and LUMO + 4 (b_2) orbitals are similar to those for the sulfido-bridged complex. The HOMO to LUMO transition is calculated to be at 566 nm (2.19 eV) and experimentally, the lowest energy band observed is centered at 645 nm (1.94 eV). The HOMO (a_1) to LUMO + 2 (b_2) and HOMO (a_1) to LUMO + 4 (b_2) transitions are predicted to occur at 509 nm (2.43 eV), and in the observed spectrum, there is a band centered at 499 nm (2.48 eV). Upon further inspection of the experimental spectrum (Fig. 3), it can be seen that there is an absorption band at 345 nm (3.59 eV) (ε = 5500) that appears as a shoulder. This absorption appears to arise from electronic transitions between Ep_π lone-pair orbitals and higher energy unoccupied metal–metal orbitals at 359 nm (3.46 eV).

In the case of the tellurido-bridged complex, the two lowest energy bands are predicted to arise from the HOMO (a′) to LUMO (a″) and HOMO to LUMO + 2 (a′) and HOMO to LUMO + 4 (a′) transitions. The LUMO + 2 (a′) and LUMO + 4 (a′) orbitals are similar to those for the selenido-bridged complex. The predicted HOMO to LUMO transition is at 582 nm (2.12 eV) and in the experimentally obtained spectrum, the λ_{max} value for the HOMO (a′) to LUMO (a″) transition is at 687 nm (1.80 eV). The HOMO (a′) to LUMO + 2 (a′) and HOMO (a′) to LUMO + 4 (a′) transitions are calculated to occur at 506 nm (2.48 eV), and these transitions are obscured due to the charge-transfer band arising from transitions between Ep_π lone-pair orbitals and higher energy unoccupied metal–metal orbitals. The charge-transfer transitions are predicted to be at 414 nm (2.99 eV), and this accounts for the apparent gain of intensity of the second absorption band (from right to left in Fig. 2) in the visible spectrum that has a λ_{max} value of 423 nm (2.93 eV). For the oxo- and sulfido-bridged complexes, these transitions are not seen in the experimentally obtained UV-visible spectra due to strong LMCT bands above 335 nm, but are predicted to be at 290 and 309 nm, respectively. The absorption bands arising from transitions between the Ep_π lone-pair orbitals and higher energy unoccupied metal–metal orbitals are red shifted down the series from O → Te. In this report, the theoretical and experimental data agree very well particularly for the visible region of the spectra where the largest difference between excitation energies is 0.32 eV or less.

The LMCT bands below 335 nm in the UV region of the spectra (Fig. 3) have not been discussed thus far and deserve a few comments. Based upon the calculations, the character of the molecular orbitals between which the transitions occur consists of σ to σ* (HOMO (a_1) to LUMO + 4) (b_2) (a′ to a′ for Te), Ep_π-based orbitals to M–M unoccupied orbitals, and terminal oxygen-based orbitals to M–M unoccupied orbitals. The calculations predict many transitions to give rise to the charge-transfer bands and complete details of the results are given in the supplementary information. The oxo-bridged complex is predicted to have charge-transfer bands, in the 302–261 nm range (4.10–4.74 eV), and two partially resolved bands are seen in the UV region having λ_{max} values of 261 and 226 nm (4.74 and 5.49 eV), respectively. Charge-transfer bands are predicted in the 353–290 nm range (3.51–4.27 eV) for the

sulfido-bridged complex, and there are two partially resolved bands observed at 284 and 265 nm (4.63 and 4.68 eV). The spectra of the selenido-bridged complex also has two partially resolved charge-transfer bands at 294 and 276 nm (4.22 and 4.49 eV) which are consitent with predicted charge-transfer bands in the 330–293 nm range (3.76–4.23 eV). The tellurido-bridged complex is predicted to have charge-transfer bands in the 362–300 nm range (3.42–4.13 eV), and again, there are two partially resolved bands at 310 and 284 nm (4.00 and 4.36 eV). Again, the experimental and calculated transition energies agree fairly well for the UV region of the spectrum where the largest difference is 0.75 eV.

To put our work in perspective, it should be noted that to date TDDFT calculations have been utilized to attain excitation energies of small organic molecules,[8] free base porphyrins,[9] fullerenes,[10] chlorophyll a,[11] and other large molecules[12] and recently, Baerends and co-workers have published two papers utilizing TDDFT calculations to assign the optical spectra of molecules containing transition metals. In the first report, the previously controversial assignment of the optical spectra of three complexes MnO_4^-, $Ni(CO)_4$ and $Mn_2(CO)_{10}$ were considered.[13] The second manuscript deals with the optical spectra of the nickel tetrapyrrole series NiP, NiPz, NiTBP and NiPc (P = porphyrins, Pz = porphyrazines, TBP = tetrabenzoporphyrins, and Pc = phthalocyanines).[14] In both papers the theoretical results agreed well with the experimental data. Our results further support the use of TDDFT for organometallic systems.

Conclusions

The addition reactions of $[W_2(OCH_2{}^tBu)_8]_n$ to produce the series of compounds $W_2(\mu\text{-}E)(\mu\text{-}OCH_2{}^tBu)_2(OCH_2{}^tBu)_6$ afford a rare opportunity to compare and contrast the bonding and electronic structure of a closely related series of Group 16 element bridged dinuclear compounds. As the chalcogenide increases in atomic number the W–E and W–W bond distance increases as can be seen in the solid state. However, in all of these compounds, there appears to be a W–W σ-bond and the DFT calculations reveal this to be the HOMO. In descending the series O → Te, the relative energy of the Ep_π atomic orbitals is raised, and this gives rise to a charge-transfer band, Ep_π to W_2, that is red shifted with increasing size of the E atom. The DFT calculations on the model compounds $W_2(\mu\text{-}E)(\mu\text{-}OCH_3)_2(OCH_3)_6$ reproduce the observed structural parameters for the $W_2(\mu\text{-}E)(\mu\text{-}OR)_2(OR)_6$ moiety within reasonable limits, and the TDDFT vertical excitation energy calculations reliably support the trends observed in the electronic absorption spectra. We think this manuscript will add to the growing body of work that shows TDDFT calculations can be a useful tool for the study of electronic absorption spectra of transition metal complexes.

Experimental

All manipulations were carried out under an inert atmosphere of oxygen-free UHP-grade argon using standard Schlenk techniques or under a dry and oxygen-free atmosphere of nitrogen in a Vacuum Atmospheres Co. Dry Lab System. Hexane was degassed and distilled from sodium–benzophenone under nitrogen. Toluene was degassed and distilled from sodium under nitrogen. Toluene-d_8 was degassed, stirred over sodium for 24 h and vacuum transferred to an ampoule. Pyridine *N*-oxide, sulfur, selenium (100 mesh), tellurium (200 mesh) and P^nBu_3 were purchased from Aldrich and were used as received. $[W_2(OCH_2{}^tBu)_8]_n$[4] and tri-*n*-butylphosphine telluride[15] were prepared according to literature procedures.

NMR spectra were recorded on 300 MHz Varian Gemini 2000 or 400 MHz Bruker DPX Avance[400] spectrometers. All ^{1}H NMR chemical shifts are reported in ppm relative to the ^{1}H impurity in toluene-d_8 at δ 2.09. UV-visible spectra were recorded as THF solutions on a Perkin-Elmer Lambda 900 spectrometer. IR spectra were recorded as Nujol™ mulls using either CsI or polyethylene windows on a Perkin-Elmer Spectrum GX spectrometer.

Syntheses

Preparation of $W_2(\mu\text{-}O)(\mu\text{-}OCH_2{}^tBu)_2(OCH_2{}^tBu)_6$. To a 25 mL round-bottomed flask was added $[W_2(OCH_2{}^tBu)_8]_n$ (0.120 g, 0.113 mmol) and pyridine *N*-oxide (0.010 g, 0.113 mmol). Toluene (10 mL) was added which gave a purple solution. The reaction mixture was stirred for 3 h at ambient temperature and then the solvent was removed under a dynamic vacuum. Recrystallization from hexanes at −20 °C gave X-ray quality purple crystals, $W_2(\mu\text{-}O)(\mu\text{-}OCH_2{}^tBu)_2(OCH_2{}^tBu)_6$, in 87% yield. ^{1}H NMR (300 MHz, toluene-d_8, 24 °C): δ 1.06 (s, 72H), 4.62 (s, 16H). ^{1}H NMR, −65 °C: δ 1.07 (18 H), 1.08 (36 H), 1.30 (18 H), 4.32 (s, 4 H), 4.67 (d, 4 H, J_{H-H} = 10.8 Hz), 4.96 (s, 4 H), 5.04 (d, 4H, J_{H-H} = 10.4 Hz). ^{13}C{^{1}H} NMR (75 MHz, toluene-d_8, 24 °C): δ 27.3 ($C(CH_3)_3$), 34.4 (CH_2). UV-vis (THF, λ_{max}/nm (ε/dm^3 mol^{-1} cm^{-1})): 586 (210), 478 (220), 261 (25 100), 226 (26 700). IR (ν_{max}/cm^{-1}): 1462 (s), 1392 (m), 1377 (m), 1362 (m), 1289 (vw), 1262 (vw), 1216 (w), 1048 (s), 1020 (s), 1010 (s), 999 (s), 934 (w), 906 (vw), 758 (w), 741 (w), 722 (w), 690 (m), 667 (m), 639 (w), 603 (w), 508 (w), 460 (w), 453 (w), 405 (w), 320 (w). Anal. Calc. for $C_{40}H_{88}O_9W_2$: C, 44.45; H, 8.21. Found: C, 44.18; H, 8.11%.

Preparation of $W_2(\mu\text{-}S)(\mu\text{-}OCH_2{}^tBu)_2(OCH_2{}^tBu)_6$. To a 25 mL round-bottomed flask was added $[W_2(OCH_2{}^tBu)_8]_n$ (0.100 g, 9.39×10^{-2} mmol) and elemental sulfur (0.003 g, 1.2×10^{-2} mmol). Hexanes (10 mL) were added which gave a purple solution. The suspension was stirred for 3 h at ambient temperature and then the solvent was removed under a dynamic vacuum. Recrystallization from hexanes at −20 °C gave X-ray quality blue crystals, $W_2(\mu\text{-}S)(\mu\text{-}OCH_2{}^tBu)_2(OCH_2{}^tBu)_6$, in 78% yield. ^{1}H NMR (300 MHz, toluene-d_8, 24 °C): δ 1.06 (s, 72 H), 4.69 (s, 16 H). ^{1}H NMR, −65 °C: δ 1.04 (s, 18H), 1.08 (s, 36H), 1.29 (s, 18H), 4.68 (s, 4H), 4.73 (d, 4H, J_{H-H} = 11.1 Hz), 4.83 (s, 4H), 4.96 (d, 4H, J_{H-H} = 10.2 Hz). ^{13}C{^{1}H} NMR (75 MHz, toluene-d_8, 24 °C): δ 27.2 ($C(CH_3)_3$), 34.8 (CH_2). UV-vis (THF, λ_{max}/nm (ε/dm^3 mol^{-1} cm^{-1})): 625 (180), 498 (340), 284 (28 500), 265 (sh, 24 100). IR (ν_{max}/cm^1): 1463.36 (s), 1391 (m), 1377 (m), 1326 (m), 1350 (w), 1304 (vw), 1287 (vw), 1260 (vw), 1217 (w), 1089 (w), 1067 (s), 1056 (s), 1018 (s), 995 (s), 981 (m), 933 (w), 754 (w), 722 (w), 685 (m), 670 (m), 654 (m), 596 (w), 458 (w), 434 (w), 400 (w), 385 (w), 333 (w), 309 (w), 292 (w). Anal. Calc. for $C_{40}H_{88}O_8SW_2$: C, 43.80; H, 8.09. Found: C, 43.31; H, 7.60%.

Preparation of $W_2(\mu\text{-}Se)(\mu\text{-}OCH_2{}^tBu)_2(OCH_2{}^tBu)_6$. To a 25 mL round-bottomed flask was added $[W_2(OCH_2{}^tBu)_8]_n$ (0.100 g, 9.39×10^{-2} mmol) and elemental Se (0.008 g, 0.1 mmol). Hexanes (15 mL) were added which gave a dark blue solution. The suspension/solution was stirred for 24 h at ambient temperature and the solvent was removed under dynamic vacuum. Recrystallization from hexanes (*ca.* 10 mL) at −20 °C gave X-ray quality crystals, $W_2(\mu\text{-}Se)(\mu\text{-}OCH_2{}^tBu)_2(OCH_2{}^tBu)_6$, in 33% yield. A second crop of crystals was isolated to increase the overall yield to 55%. ^{1}H NMR (300 MHz, toluene-d_8, 24 °C): δ 1.06 (s, 72H), 4.68 (s, 16H). ^{1}H NMR, −85 °C: δ 1.07 (s, 18H), 1.09 (s, 36H), 1.30 (s, 18H), 4.50 (s, 4H), 4.85 (d, 4H, J_{H-H} = 10.5 Hz), 4.91 (s, 4H), 4.99 (d, 4H, J_{H-H} = 10.2 Hz). ^{13}C{^{1}H} NMR (300 MHz, toluene-d_8, 24 °C): δ 27.89 ($C(CH_3)_3$), 35.43 (CH_2). UV-vis (THF, λ_{max}/nm (ε/dm^3 mol^{-1} cm^{-1})): 645 (210), 499 (330), 345 (5500), 294 (20 100), 276 (18 300). IR (ν_{max}/cm^{-1}): 1464 (s), 1391 (m), 1377 (m), 1362 (m), 1350 (w), 1287 (vw), 1260 (vw), 1216 (w), 1068 (s), 1057 (s), 1042 (s), 1023 (m), 1017 (s), 992 (s), 977 (m), 933 (w),

906 (vw), 754 (w), 722 (w), 682 (m), 668 (m), 652 (m), 595 (w), 472 (w), 458 (w), 419 (w), 398 (w), 328 (w). Anal. Calc. for $C_{40}H_{88}O_8Se_1W_2$: C, 42.00; H, 7.75. Found: C, 41.73; H, 7.66%.

Preparation of $W_2(\mu\text{-Te})(\mu\text{-OCH}_2{}^t\text{Bu})_2(\text{OCH}_2{}^t\text{Bu})_6$. To a 25 mL round-bottomed flask was added Te (0.13 g, 0.1 mmol), P^nBu_3 (25.4 μL, 0.1 mmol) and toluene (5 mL). This solution was stirred for *ca*. 30 min at which point most of the tellurium powder had dissolved and the solution color was light yellow. Another 25 mL round-bottomed flask was charged with $[W_2(OCH_2{}^tBu)_8]_n$ (0.100 g, 0.1 mmol) and toluene (15 mL) and the resulting solution was added drop-wise to the first flask containing the $^nBu_3PTe$ and toluene. The resulting solution was dark yellow and was stirred for 24 h. Filtration through a medium glass frit with a Celite pad gave a clear dark yellow solution. The solution was concentrated until *ca*. 10 mL of toluene remained and a precipitate was visible. The solution was then heated to 80 °C in a hot oil bath to re-dissolve the precipitate and then the solution was allowed to cool slowly in the oil bath to ambient temperature. Over a period of 24 h, dark crystals were deposited and identified as $W_2(\mu\text{-Te})(\mu\text{-OCH}_2{}^t\text{Bu})_2(\text{OCH}_2{}^t\text{Bu})_6$ in 41% yield. ^{1}H NMR (400 MHz, toluene-d_8, 27 °C): δ 1.10 (s, 72H), 4.66 (s, 16H). ^{1}H NMR, −60 °C: δ 1.04 (s, 18H), 1.05 (s, 36H), 1.26 (s, 18H), 4.09 (s, 4H), 4.88 (d, 4H, J_{H-H} = 10.8 Hz), 4.89 (s, 4H), 4.93 (d, 4H, J_{H-H} = 10.8 Hz). ^{13}C{^{1}H} NMR (400 MHz, toluene-d_8, 27 °C): δ 27.59 ($C(CH_3)_3$), 35.14 (CH_2). UV-vis (THF, λ_{max}/nm (ε/dm^3 mol^{-1} cm^{-1})): 687 (300), 423 (5500), 310 (20 500), 284 (20 800). IR (ν_{max}/cm^{-1}): 1463 (s), 1458 (s), 1390 (w), 1377 (m), 1362 (m), 1349 (w), 1287 (vw), 1260 (vw), 1216 (vw), 1070 (s), 1062 (s), 1041 (s), 1017 (s), 987 (m), 972 (m), 933 (w), 754 (w), 677 (m), 668 (m), 649 (m), 592 (vw), 474 (vw), 457 (w), 419 (w), 398 (w), 328 (w). Anal. Calc. for $C_{40}H_{88}O_8Te_1W_2$: C, 40.29; H, 7.44. Found: C, 40.39; H, 7.47%.

Crystallography

For the oxo-bridged complex a single crystal of suitable size was obtained by cleaving a larger crystal in a nitrogen filled glove bag. The crystal was attached to a glass fiber using silicone grease and was transferred to the goniostat where it was cooled to 108 K. A preliminary search for peaks and analysis using the programs DIRAX[16a] and TRACER[16b] revealed a triclinic unit cell. The choice of the centrosymmetric space group $P\bar{1}$ was confirmed by the subsequent solution and refinement of the structure. Unit cell dimensions were determined by an unrestrained least-squares fit of the setting angles for 60 carefully centered reflections having 2θ values between 25 and 35°. After correction for absorption *via* the analytical face-indexed technique of de Meulenaer and Tompa,[16c] data processing gave a unique set of 6890 reflections and the merging R(avg.) = 0.019 for the averaging of 3362 reflections measured more than once. Plots of the four standard reflections (−5 0 0, 0 0 −6, 2 6 −2, 0 10 0) measured every 200 reflections showed no significant trends.

The structure was solved using a combination of direct methods (MULTAN-78)[16d] and difference Fourier techniques. The positions of the two tungsten atoms were obtained from the initial E-map. The remaining non-hydrogen atoms were located in iterations of least-squares refinement followed by a difference Fourier calculation. Almost all of the hydrogen atoms were evident in a later difference map. For the final cycles of full matrix least-squares refinement hydrogen atoms were included in fixed calculated positions with isotropic thermal parameters equivalent to 1.0 plus the isotropic equivalent of the parent atom. The non-hydrogen atoms were refined using anisotropic thermal parameters. The final $R(F)$ was 0.023 for 461 variables and the full unique data. Data having $F < 3\sigma(F)$ were given zero weight.

The final difference map was essentially featureless, the largest peak was 1.64 e Å^{-3} in the vicinity of a tungsten atom and the deepest hole was −0.75 e Å^{-3}.

For the sulfido-bridged complex a single crystal was obtained by cleaving a large dark blue piece of the sample in a nitrogen filled glove bag. The crystal was attached to a glass fiber using silicone grease and was transferred to the goniostat where it was cooled to 108 K. A preliminary search for peaks and analysis using the programs DIRAX[16a] and TRACER[16b] revealed a primitive triclinic unit cell. The choice of the centrosymmetric space group $P\bar{1}$ was confirmed by the subsequent solution and refinement of the structure. Unit cell dimensions were determined by an unrestrained least-squares fit of the setting angles for 26 carefully centered reflections having 2θ angles between 19 and 21°. After correction for absorption *via* the analytical face-indexed technique of de Meulenaer and Tompa,[16c] data processing gave a unique set of 6376 reflections and the merging R(avg.) = 0.022 for the averaging of 2383 reflections that had been measured more than once. Plots of the four standard reflections (0 0 4, −4 0 0, 0 4 0, −4 4 1) measured every 400 reflections showed no significant trends.

The structure was solved using a combination of direct methods (MULTAN-78)[16d] and Fourier techniques. The positions of the tungsten atoms were obtained in the initial E-map. The remaining non-hydrogen atoms were located in iterations of least-squares refinement followed by difference Fourier calculation. Almost all of the hydrogen atoms were located after initial refinement of the complete molecule; at least one was found in each of the methyl groups. For the final cycles of least-squares refinement the hydrogen atoms were included in fixed idealized positions with isotropic thermal parameters fixed at one plus the isotropic equivalent of the parent atom. The non-hydrogen atoms were refined using anisotropic thermal parameters. The final $R(F)$ was 0.029 for 461 variables and using all of the unique data. Data having $F < 3\sigma(F)$ were given zero weight.

The final difference map was essentially featureless, the largest peak was 1.9 e Å^{-3} in the vicinity of W(1) and the deepest hole was −0.92 e Å^{-3}.

The data for the selenido- and tellurido-bridged complexes were collected on a Bruker Platform goniometer equipped with a SMART 6000 CCD detector. Frames were measured for 10 s each with a frame width of 0.3° in Ω. Seven 180° frame runs were measured, each at a different phi position, and the first 50 frames were re-measured at the end of the data collection. Frames were processed and integrated with the use of Bruker's SAINT[16e] software, and reflections out to a maximum of 60° in 2θ were harvested.

The crystals were twinned, as were all others of the same samples that were examined. The twinning was resolved with the use of Bruker's Gemini software, version 1.02.[16f] In this way, the diffraction data were found to have triclinic symmetry and no systematic absences. Successful structure solution and refinement confirmed the choice of the centrosymmetric space group alternative, $P\bar{1}$.

Data were corrected for absorption *via* the semi-emperical technique of the program SADABS.[16g] Identically indexed reflections were averaged. Those data that were not overlapped and those that were completely overlapped were selected for structure solution and refinement. For the selenido-bridged compound the merging R(avg.) = 0.064 and for the telluride-bridged compound the merging R(avg.) = 0.075. The structure was solved by direct methods and completed by Fourier techniques. Hydrogen atoms were placed in calculated positions and refined with the use of a riding model in the final cycles of least squares. The tungsten, selenium and tellurium atoms were refined anisotropically, and all other atoms were refined isotropically. The final difference electron density map for the selenido-bridged compound had the largest peak with an intensity of 1.74 e Å^{-3} and was located near the sites of C(35) and

H(35A) and for the tellurido-bridged compound the final difference electron density map had the greatest peak with an intensity of 1.08 e $Å^{-3}$ and located near the sites of C(7) and H(7B).

CCDC reference numbers 158778–158781.

See http://www.rsc.org/suppdata/dt/b1/b101346g/ for crystallographic data in CIF or other electronic format.

Gaussian 98 DFT calculations

Density functional theory (DFT)[17] calculations with the Gaussian 98 suite of programs[18] utilized the B3LYP[19–21] method and standard basis sets.[22] C, H, O, and S were described with the 6-31G* basis set (and 5 'pure' d functions), while W,[23] Se[24] and Te[24] were represented by an SDD effective core potential. All geometries for the O, S, and Se complexes were fully optimized at this level under C_{2v} symmetry using the default optimization criteria. The tellurido-bridged complex having C_s symmetry was considered optimized when the total energy (in Hartrees) of the molecule stopped changing in the fifth decimal place. Orbital analyses were completed with the GaussView[25] program

Acknowledgements

We thank the National Science Foundation for support and the Ohio Supercomputer Center for computational resources with which the electronic structure calculations were performed.

References

1 F. A. Cotton and R. A. Walton, *Multiple Bonds Between Metal Atoms*, Oxford University Press, 2nd edn., 1993.
2 C. P. Casey, R. S. Carino, R. K. Hayashi and D. K. Schadesky, *J. Am. Chem. Soc.*, 1996, **118**, 1617.
3 M. R. Burke and J. Takats, *J. Organomet. Chem.*, 1986, **302**, C25.
4 T. A. Budzichowski, M. H. Chisholm, K. Folting, J. C. Huffman and W. E. Streib, *J. Am. Chem. Soc.*, 1995, **117**, 7429.
5 (*a*) D. C. Swenson and L. Messerle, *Inorg. Chem.*, 1998, **37**, 3257; (*b*) S. I. Troyanov, E. M. Snigireva and M. V. Lomonosova, *Zh. Neorg. Khim.*, 2000, **45**(4), 652.
6 (*a*) M. H. Chisholm, W. E. Streib, D. B. Tiedtke and D.-D. Wu, *Chem. Eur. J.*, 1998, **4**, 1470; (*b*) D. B. Tiedtke, Ph.D. Thesis, Indiana University, 1997; (*c*) M. H. Chisholm, K. Folting, M. A. Lynn, W. E. Streib and D. B. Tiedtke, *Angew. Chem., Int. Ed. Engl.*, 1997, **36**, 52.
7 (*a*) R. Bauernschmitt and R. Ahlrichs, *Chem. Phys. Lett.*, 1996, **256**, 454; (*b*) R.E. Stratmann, G. E. Scuseria and M. J. Frisch, *J. Chem. Phys.*, 1998, **109**, 8218.
8 K. B. Wiberg, R. E. Stratmann and M. J. Frisch, *Chem. Phys. Lett.*, 1998, **297**, 60.
9 S. J. A. van Gisbergen, A. Rosa, G. Ricciardi and E. J. Baerends, *J. Chem. Phys.*, 1999, **111**, 2499.
10 (*a*) S. J. A. van Gisbergen, J. G. Snijders, G. Ricciardi and E. J. Baerends, *Phys. Rev. Lett.*, 1997, **78**, 3097; (*b*) R. Bauernschmitt, R. Ahlrichs, F. H. Hennrich and M. K. Kappes, *J. Am. Chem. Soc.*, 1998, **120**, 5052.
11 D. Sundholm, *Chem. Phys. Lett.*, 1999, **302**, 480.
12 R. Bauernschmitt, M. Häser, O. Treutler and R. Ahlrichs, *Chem. Phys. Lett.*, 1997, **264**, 573.
13 S. J. A. van Gisbergen, J. A. Groeneveld, A. Rosa, G. Ricciardi and E. J. Baerends, *J. Phys. Rev. A*, 1999, **103**, 6835.
14 S. J. A. van Gisbergen, A. Rosa, G. Ricciardi and E. J. Baerends, *J. Chem. Phys. A*, 2001, **105**, 3311.
15 R. A. Zingaro, B. Steeves and K. Irgolic, *J. Organomet. Chem.*, 1965, **4**, 320.
16 (*a*) A. J. M Duisenberg, *J. Appl. Crystallogr.*, 1992, **25**, 92; (*b*) S. L. Lawton and R. A. Jacobson, Ames Research and Development Report, U.S.A.E.C. IS-1141, 1965; (*c*) J. de Meulenaer and H. Tompa, *Acta Crystallogr.*, 1965, **19**, 1014; (*d*) P. Main, S. E. Hull, L. Lessinger, G. Germain, J. P. Declerq and M. M. Woolfson, MULTAN-78: A System of Computer Programs for the Automatic Solution of Crystal Structures from X-Ray Diffraction Data, Universities of York, UK, and Louvain, Belgium, 1978; (*e*) SAINT, ver. 4, Siemens Analytical X-Ray Systems, Inc., Madison, WI, 1996; (*f*) Gemini Twinning Solution Program Suite, ver. 1.02, Bruker AXS, Inc., 2000; (*g*) G. M Sheldrick, SADABS: Siemens Area Detector ABSorption correction program, Siemens Industrial Automation, Inc., 1996.
17 R. G. Parr and W. Yang, *Density-functional Theory of Atoms and Molecules*, Oxford University Press, 1989; J. K. Labanowski and J. W. Andzelm (Editors), *Density Functional Methods in Chemistry*, Springer-Verlag, 1991.
18 M. J. Frisch, G. W. Trucks, H. B. Schlegel, G. E. Scuseria, M. A. Robb, J. R. Cheeseman, V. G. Zakrzewski, J. A. J. Montgomery, R. E. Stratmann, J. C. Burant, S. Dapprich, J. M. Millam, A. D. Daniels, K. N. Kudin, M. C. Strain, O. Farkas, J. Tomasi, V. Barone, M. Cossi, R. Cammi, B. Menuucci, C. Pomelli, C. Adamo, S. Clifford, J. Ochterski, G. A. Pertersson, P. Y. Ayala, Q. Cui, K. Morokuma, D. K. Malick, A. D. Rabuck, K. Raghavachari, J. B. Foresman, J. Cioslowski, J. V. Ortiz, A. G. Baboul, B. B. Stefanov, G. Liu, A. Liashenko, P. Piskorz, I. Komaromi, R. J. Gomperts, R. L. Martin, D. J. Fox, T. Keith, M. A. Al-Lahman, C. Y. Peng, A. Nanayakkara, M. Challacombe, P. M. W. Gill, B. Johnson, W. Chen, M. W. Wong, J. L. Andres, C. Gonzalez, M. Head-Gordon, E. S. Replogle and J. A. Pople, Gaussian 98 Version A9, Gaussian Inc., Pittsburgh, PA, 1998.
19 A. D. Becke, *Phys. Rev. A*, 1988, **38**, 3098.
20 A. D. Becke, *J. Chem. Phys.*, 1993, **98**, 5648.
21 C. Lee, W. Yang and R. G. Parr, *Phys. Rev. B*, 1988, **37**, 785.
22 W. J. Hehre, L. Radom, P. v. R. Schleyer and J. A. Pople, *Ab initio Molecular Orbital Theory*, John Wiley & Sons, New York, 1986.
23 D. Andrae, U. Haeussermann, M. Dolg, H. Stoll and H. Preuss, *Theor. Chim. Acta*, 1990, **77**, 123.
24 J. M. Martin and A. Sundermann, *J. Chem. Phys.*, 2001, **114**, 3408.
25 GaussView 2.1, Gaussian Inc., Pittsburgh, PA, 1998.
26 M. N. Burnett and C. K. Johnson, ORTEP III: Oak Ridge Thermal Ellipsoid Plot Program for Crystal Structure Illustrations, Oak Ridge National Laboratory Report, ORNL-6895, 1996.